

Ligament mediated aerobreakup of a droplet

Saini Jatin Rao and Saptarshi Basu*

Department of Mechanical Engineering, Indian Institute of Science, Bangalore 560012, India

(Dated: February 11, 2025)

Droplet formation is relevant in a multitude of applications spanning natural and artificial settings. Comprehending droplet aerobreakup or air-assisted secondary atomization is challenging, especially in high-speed flow scenarios. This entails multi-scale interface deformations with intricate wave dynamics that conform to a non-linear cascade. In the present study, we look into shockwave-induced breakups and associated intermediate processes happening at a smaller spatiotemporal scale over the disintegrating droplet interface at different Weber numbers ($We \sim 10^3$). We observe the undulations to follow breakup patterns that resemble a scaled-down version of a secondary atomization event. These sub-secondary breakup processes end with corrugated ligaments that generate the final daughter droplets. The size distribution of these droplets is estimated using a Depth from Defocus (DFD) technique. These illustrate the transient nature of aerobreakup, where the normalized statistics in subsequent time periods and different We are observed to follow a common underlying distribution. This conforms to a gamma distribution where the associated fit parameters agree well with the coefficients determined from ligament shape factors, corresponding to the limit associated with most extreme corrugations. Scaling laws based on We are deduced for the averaged statics using a high energy chaotic breakup mechanism. These observations reinforce the idea of a self-similar mechanism for the catastrophic aerobreakup of a droplet.

I. INTRODUCTION

When subjected to aerodynamic forcing from high-speed gas flows, a liquid drop undergoes rapid destabilization and fragmentation into many tiny daughter droplets. This process of generating droplets or secondary atomization is relevant in many practical scenarios ranging from aerospace applications, spray coating systems, and powder production for pharmaceutical, food, or additive manufacturing applications [1]. An interactive evolution of disruptive and resistive forces establishes the breakup dynamics. The Weber number ($We = \rho_a u_a^2 d_0 / \sigma$) denotes the balance between aerodynamic and capillary forces; and Ohnesorge number ($Oh = \mu_l / \sqrt{\rho_l \sigma d_0}$) illustrates relative dominance of viscous effects over surface tension. Here d_0 is the initial droplet diameter, u_a is the free stream air velocity, σ is the surface tension, ρ is the density and μ is the viscosity where subscripts a and l represent air (gas) and liquid respectively. These dimensionless numbers are sufficient to predict various aspects of this multi-faceted problem [1–3]. The disintegrating droplet illustrates identifiable intermediate topologies, which represent different breakup modes. These modes can be delineated on a We-Oh regime map. The older convention established modes like: vibrational, bag, multi-mode, stripping and catastrophic breakup [2]. However, recent advances illustrated the significant role of interfacial instabilities, hence, reclassifying the breakup modes to Rayleigh-Taylor Piercing (RTP) and Shear-Induced Entrainment (SIE) [3]. The deforming droplet interface, where the lighter fluid (air) accelerates into the denser fluid (liquid), is destabilized through a Rayleigh-Taylor instability (RTI). This leads to RTP mode and formation of rim and bags over the deformed droplet. At higher We, the aerodynamic shear on the forward facing segment of the droplet interface is significant, inducing a Kelvin-Helmholtz instability (KHI) and SIE mode. The KHI waves mediate the liquid transport along the periphery or a stripping process. The liquid is stripped in the form of sheets, ligaments and droplets. This particular stripping process and the associated non-linear evolution of interface is discussed in this paper. The KHI in the non-linear regime undergoes subsequent destabilization through other unstable mechanisms forming a wave cascade, that we will discuss below. This cascading behavior is observed in primary atomization as well. A temporal evolution of the liquid structure length scale depicted a cascade with diminishing scales [4]. The average radius of curvature of the interface increases with time as well, indicating the formation of corrugated ligaments. This cascade behavior was explained using a vortex dynamics approach [5, 6]. A regime map for topological evolution of the local wave features was deduced based on global flow parameters. Furthermore, a recent study [7] presented the undulation breakup over the destabilized jet surface to be analogous to secondary atomization and defined a local We to establish a regime map. The observed modes were morphologically similar to the droplet breakup modes at lower We.

These sub-scale processes associated with atomization events end with ligament-mediated mechanism. Several studies emphasized the role of these ligament in final droplet production through the Rayleigh-Plateau instability

* Contact author: sbasu@iisc.ac.in

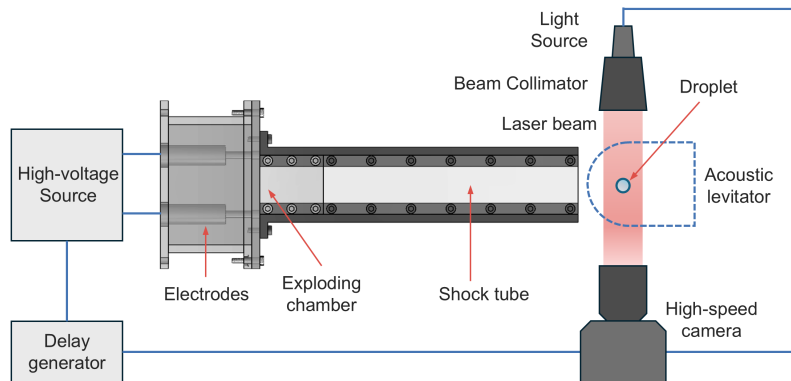


FIG. 1. Experimental setup illustrating a wire-explosion based shock tube, actuated by a pulsed high voltage source. An acoustic levitator is used to place the droplet at the opening. A shadowgraphy system is deployed for imaging.

(RPI). The geometric characteristic of the ligament determine the the size of distribution of the daughter droplets. Based on an model considering aggregation of possible breakup and coalescence events of the sub-elements of the ligament (imagining ligament to be constituted of blobs matching the local diameter), a correlation was established between the shape factor and coefficients of the gamma distribution associated with final droplet sizes [8]. This can also be extended to determine parameters of a compound gamma distribution [9]. Furthermore, this mechanism was extended to non-Newtonian liquids and a limit over these coefficients corresponding to extreme levels of corrugation were also established [10]. We intend to extend these ideas to droplet aerobreakup and assess the sub-scale breakup events of the undulations or the self-similar sub-secondary atomization processes. These processes terminate with corrugated ligaments. In these extreme flow condition of shock-induced atomization, we observe the ligament shape factors and the associated daughter droplet size distribution to correspond to extreme corrugation limit. This enables us to move towards a self-similar model for droplet disintegration in the catastrophic breakup regime.

II. EXPERIMENTAL SETUP AND METHODS

An exploding-wire-based shock tube setup was used for the shock-droplet interaction experiments, as illustrated in Fig. 1. Details for the same can be found in the previous works [11–13], however, the essential details will be briefly discussed here. A high-voltage source (2kJ pulse power, Zeonics Systech India, Z/46/12) is used to discharge electrical energy through a thin wire (35 SWG, bare copper wire) for a very short time duration ($\sim O(1)\mu s$), causing an explosion accompanied by a blast wave. This is transformed into a planar shock wave by deploying a rectangular shock tube cavity ($20mm \times 40mm \times 320mm$). An isolated DI water droplet of size $d_0 \approx 2mm$ is positioned at the opening of the shock tube using an acoustic levitator. A digital delay generator (BNC 575) simultaneously triggers the imaging and shock tube system. The shock Mach numbers (Ma_s) are controlled by adjusting the charging voltage (V_c). Experiments are carried out at $Ma_s = 1.27, 1.39$ & 1.56 , with corresponding Weber numbers $We \approx 900, 2000$ & 4000 [14].

In the current exposition, shadow imaging is realized by using a Cavitar Cavilux smart UHS pulsed laser connected to a beam expander and a diffuser plate for uniform background illumination. The images were captured at $75kHz$ ($93kHz$ for some instances) using a Photron SA5 camera. A $6.5\times$ Navitar zoom lens coupled with a $1.5\times$ attachment and $2\times$ objective ensured a resolution of $2.38\mu m/\text{pixel}$. A modified version of this imaging system was deployed earlier in the previous study [14] to determine the daughter droplet sizes using the Depth from Defocus (DFD) approach. A higher magnification optical configuration, a beam splitter, and two high-speed cameras were used to acquire two simultaneous images with different extents of blurring. The sizing statistics hence obtained earlier are subsequently assessed here for further insights into the fragmentation process.

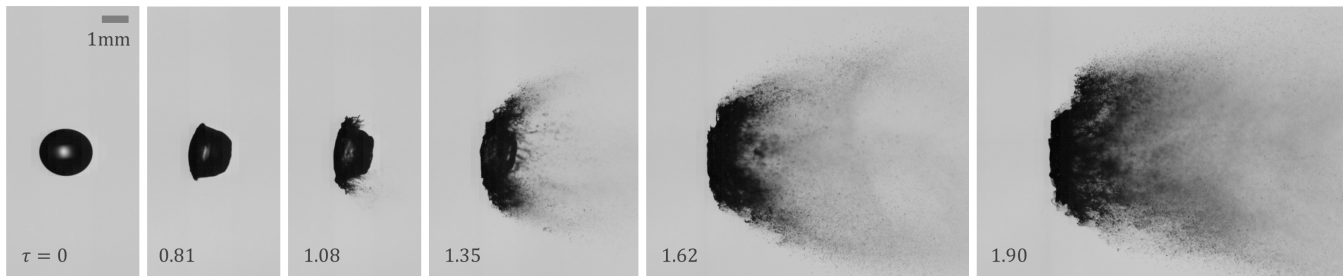


FIG. 2. Shock induced breakup of a droplet at $We \approx 2000$, depicting an Shear-Induced Entrainment (SIE) mode.

III. RESULTS AND DISCUSSION

A. Global overview

A global view of the shock droplet interaction at a $We \approx 2000$ is depicted in Fig. 2. The time stamps are clocked from the moment shockwave interacts with the droplet, and it is normalized with the inertial time scale $t_i = d_0/u_a \sqrt{\rho_a/\rho_l}$ such that $\tau = t/t_i$. In this regime, we observe a SIE mode of breakup. The shock wave has a minimal influence on the droplet [11], and the induced flow imposes aerodynamic disruptive forces. The drop starts deforming in the presence of non-uniform shear and pressure imposition on the surface. It takes up a cup-cake shape with a lip-like feature at the equator by virtue of shear and wake vortices [11]. Shear on the forward-facing segment induces liquid mass transport to the periphery, which is accompanied by unstable waves originating from KHI. This liquid is then stripped off through the imposition of other unstable wave modes, which will be discussed below. However, to crudely describe, the KHI wave crest are destabilized under the influence of local acceleration, and an azimuthal RTI enables periodic ligament formation. These ligaments then generate a fine mist of droplets through RPI, as observed in Fig. 2.

B. Sub-secondary breakup processes

In aerobreakup, a globally deforming droplet interface sets up the stage for further unstable mechanisms to manifest. In the SIE breakup mode, a shear-driven KHI generates periodic perturbations to the interface (wave crests) with characteristic wavelength and growth rates [15]. In other words, there is a characteristic spatiotemporal signature associated with these local undulations to the evolving liquid boundary. Further evolution of these undulations constitutes a sub-secondary breakup process and will be discussed in this section.

The shear induces KHI, and the deforming droplet interface imposes acceleration-induced RTI. Both of these mechanisms create undulations over the interface. The wavelength and amplitude represent the length scale of deformation. The wavelength can be deduced using linear stability analysis, enforcing simplistic assumptions but enabling reliable estimates [11, 16, 17]. The wavelength should be smaller than the droplet for it to manifest over the surface [11, 13]. Also, the growth rate of the wave amplitudes sets up a race among various modes with faster growth rates supporting early appearance. These sets a scale-based compatibility criteria. These wave crests are reminiscent of a local undulation over the interface and will be treated as a sub-scale mass of liquid body.

When exposed to extremely high-speed gas flows, these undulations disintegrate, resembling a portion of an independent fluid blob as illustrated in Fig. 3. This enables the stripping of liquid mass from the parent droplet body in a recurrent fashion [18]. The fresh surface then undergoes the next cycle of deformation, setting up an undulation again and undergoing a sub-secondary breakup process.

Ligament mode: The traverse elongation of the wave crest, associated with the growth rate of the primary wave, say KHI, establishes an acceleration-induced body force. With the heavier fluid pushing rapidly into the lighter fluid, RTI generates the azimuthal wave perturbations over this crest. The continued presence of the transverse acceleration leads to a further augmentation of these RTI wave crests, which eventually elongate with aerodynamic assistance to form ligaments [19]. These ligaments undergo an RPI mediated breakup into daughter droplets as illustrated in Fig. 3a and 4a.

However, there is another possible mechanism. The unsteady expansion of sheets is shown to be bound by unstable rims. The local undulation growing transversely can also evolve into a sheet as they stretch. The presence of a rim at the leading end of this sheet-like feature is difficult to visualize from shadowgraphy images at this early stage. However, if present, the unsteady sheet expansion induces a combined RTI-RPI effect where droplets are shed through

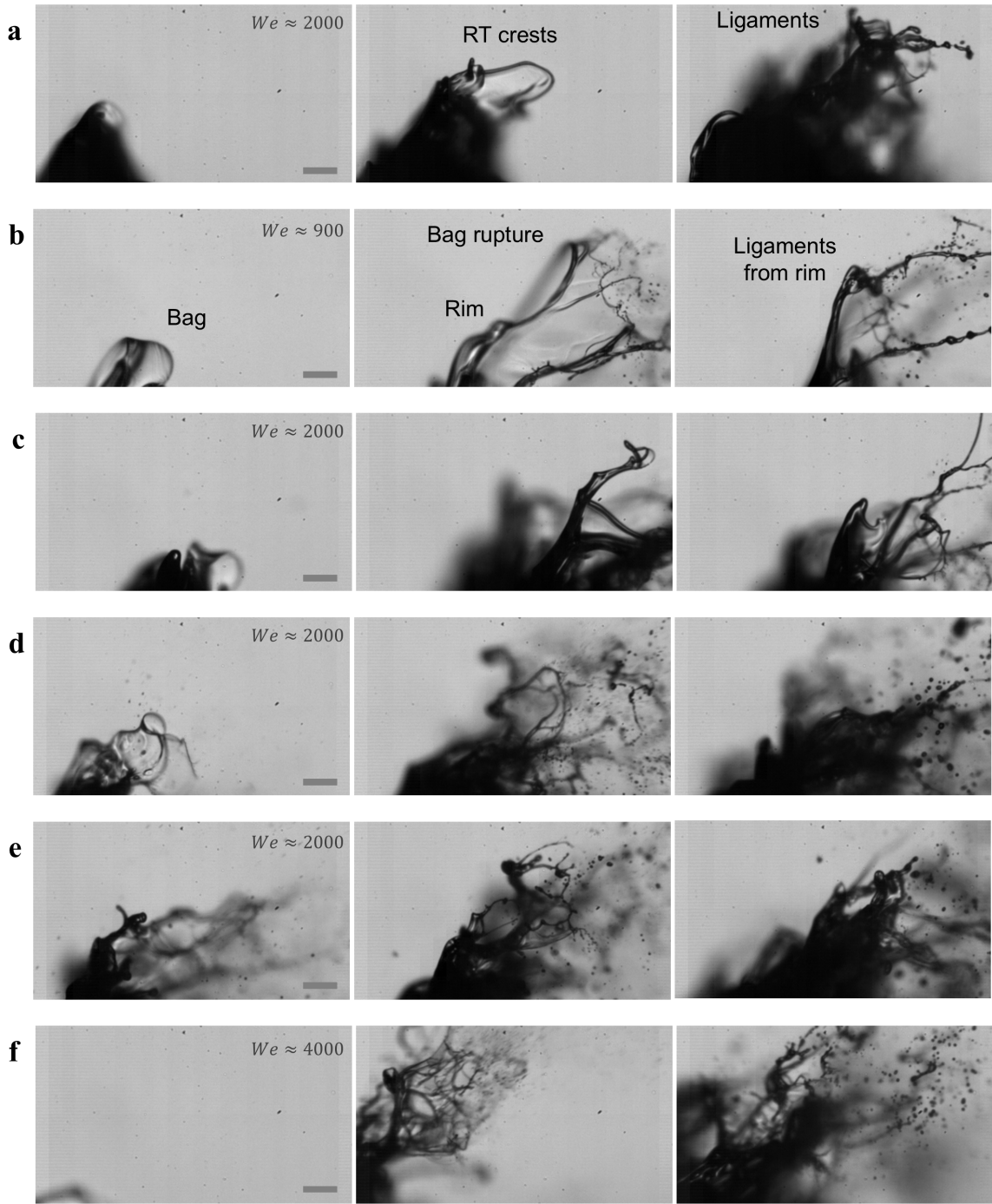


FIG. 3. Evolution of an undulation over droplet surface undergoing sub-secondary breakup processes (a) ligament mode (b-f) bag mode. The scale bar represents $100\mu\text{m}$ and consecutive frames are separated by an interval of $\Delta t = 13.33\mu\text{s}$.

periodic ligaments from the rim [20].

Bag Mode: Another possible effect arises from the drag forces over this undulation. This undulation resembles a protrusion over the liquid surface with a bluff body-like flow around. This is similar to aerodynamic forcing over the droplet. Aerobreakup of droplets shows axisymmetric dynamics subsuming a bi-fold symmetry, dividing it into two equal halves. The undulation resembles one such half [7]. The flattening of undulation under such effects, including growth in the transverse direction, leads to the formation of sheet-like features. The drag augments the acceleration imparted over the interface in the longitudinal (gas flow) direction. This imparts RTI over this sheet in the azimuthal

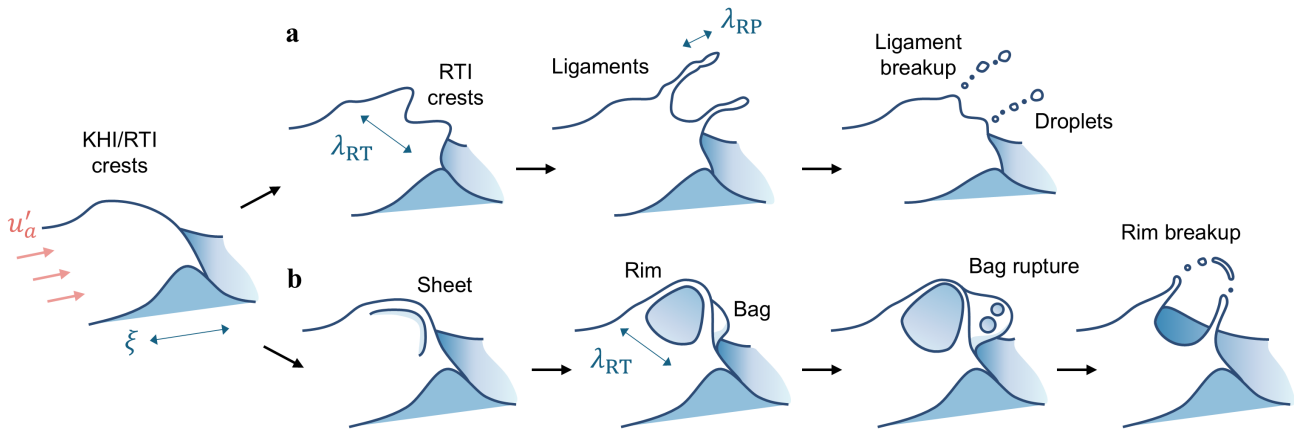


FIG. 4. Schematic illustrating sub-secondary breakup processes. The early stage KHI initiates an undulation with characteristic scale $\xi \sim \lambda_{KH}$. Beyond a particular finite amplitude, this undergoes destabilization governed by subsequent wave mechanisms, forming a non-linear wave cascade. The accelerating interface undergoes azimuthal RTI. (a) ligament mode: transverse acceleration RTI (b) bag mode: longitudinal acceleration RTI. This eventually creates terminal ligaments that generate droplets through RPI.

direction, forming bags bound by the rim. The bag grows, and the thin film ruptures, creating very fine droplets. The residual ligament fragments under the combined effect of capillary and aerodynamic forces. The rims resemble a loop, which opens up as it breaks with the base, resembling independent ligaments emerging from the parent droplet body (similar to the previous case) [21]. Refer to Figures 3b-f for observations and 4b for the schematic. This bag mode is similar to the RTP mode or bag breakup in secondary atomization [22, 23].

Similar modes or local breakup topologies were also reported in formation of sea sprays [24, 25]. In both of these sub-secondary processes, the RTI mechanism establishes a topology that evolves into ligaments that break up through aerodynamically assisted capillary breakups. However, the ligament mode has a prominent transverse acceleration, and the bag mode illustrates the same in the longitudinal direction. The bag mode also involves an additional bag film breakup, generating very small droplets. A higher inertia is required for this drag to manifest as waves and initiate bag mode. Hence we observe an abundant occurrence of bag mode in this high $We-Re$ regime of present experiments, with a very rare sight of ligament mode as evident in Fig. 3.

There are many undulations present over droplet interface simultaneously fragmenting through aforementioned sub-secondary processes. Such interactions lead to the appearance of extremely corrugated ligaments in complex groups. They sometimes appear as part of a complex web or network attached to the parent droplet segments (see Fig. 5). Another fascinating observation includes the mushroom-shaped short ligaments or blobs resembling the remnant stamen observed in the bag-stamen breakup modes (see last row of Fig. 5). Transversely stretched ligaments aligned perpendicular to the gas flow are subjected to drag and deformation-induced accelerations. The RTI breakup of ligaments consists of periodic nodes that are left behind, depicting a mushroom shape as illustrated in Fig. 6. They are similar to nodes observed over the rim (including stamen) that appear during the bag breakup of a droplet [22, 26].

Effective local dimensionless parameters: The cascades originate for instance from each KHI wave crest to finite amplitude and terminate into daughter droplets as depicted in Fig. An effective Weber number can be defined locally for this based on deformation scale ξ and local effective gas flow velocity u'_a as

$$We' \sim \frac{\rho_a u'_a{}^2 \xi}{\sigma} \quad (1)$$

A similar hypothesis bridged primary and secondary atomization events, where undulations over a destabilized liquid jet during breakup were treated as an equivalent droplet segment [7]. Based on the local effective We , the breakup dynamics were predicted for each undulation, drawing inspiration from secondary atomization. The same philosophy is extended here, and is expected to predict the modes associated with sub-secondary breakup process. Earlier studies for primary atomization [5] developed a regime map for potential modes of undulation breakup based on global dimensionless parameters. However, a local dimensionless parameter presents a self-similar approach. For viscous or non-Newtonian fluids, other relevant dimensionless numbers can be defined as well, based on these local scales. Hence We' enable predict the evolution of undulation via the ligament or bag mode discussed earlier. However determining this We' is beyond the experiment capabilities of the present study.

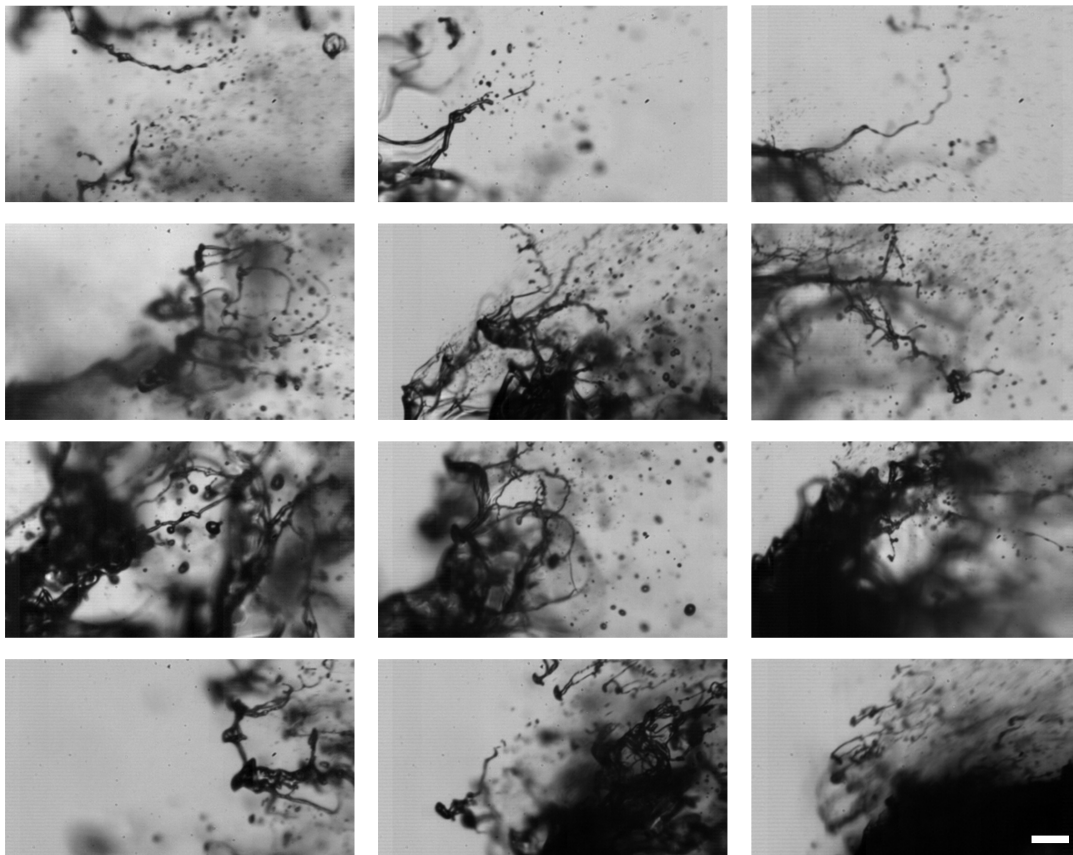


FIG. 5. Corrugated ligaments: Various ligaments observed during the aerobreakup exhibit intricate topologies and significant levels of corrugations. This catalog presents examples of ligaments that remain attached to the parent droplet or sheet or bag, as well as those that are free-standing, including mushroom-shaped blobs. Additionally, it includes intra-body ligaments and complex ligament networks that are reminiscent of a web structure. The scale bar (bottom right) represents $100\mu m$. The columns from left to right corresponds to $We \approx 900, 2000, 4000$

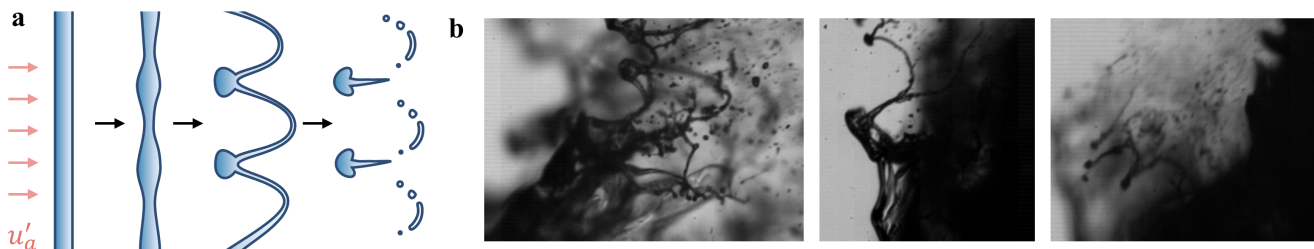


FIG. 6. RTI based Ligament breakup mechanism. (a) Schematic depicting the formation of nodes, which remain as “mushroom” blobs at the end. (b) Experimental images.

C. Ligament-mediated droplet generation

As explained earlier, the sub-secondary breakup processes ends as the undulation disintegrates into daughter droplets. However, the termination entails a final ligament-mediated mechanism. The corrugated ligaments portrays an inertio-capillary system with liquid inertia and surface tension forces dominating the dynamics. The ligament can be considered as a collection of a protoblobs where the evolution ensure two possibilities: either the blobs separate through RPI mechanism or they coalesce into a bigger blob. Recent studies [8, 10, 27] considered these effects and emphasized the role of corrugations on this delicate balance between breakup and coalescence. Hence a correlation between the ligament shape and the final daughter droplet size distribution has been established in the form of a

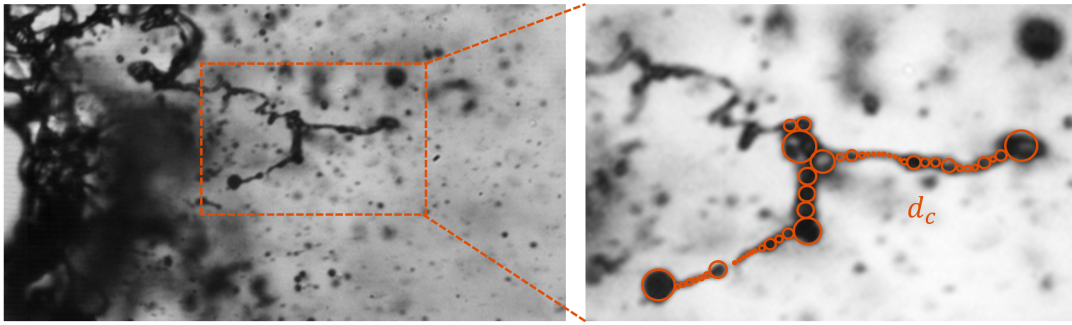


FIG. 7. A typical corrugated ligament decomposed into blobs (marked as circles) matching local ligament diameter d_c

Gamma distribution [8] or possibly a compound gamma distribution [9]

$$P_{m,n}(x = d/\langle d \rangle) = \frac{2(mn)^{(m+n)/2} x^{(m+n)/2-1}}{\Gamma(m)\Gamma(n)} \mathcal{K}_{m-n}(2\sqrt{mnx}) \quad (2)$$

where Γ is the gamma function, \mathcal{K} is the modified Bessel function of the second kind and the coefficients m and n represent ligament size distribution and corrugations. $n = \langle d_c \rangle^2 / (\langle d_c^2 \rangle - \langle d_c \rangle^2)$ is deduced by decomposing a corrugated ligament into blobs matching local ligament diameter d_c as illustrated in Fig. 7. $m = \langle l \rangle^2 / (\langle l^2 \rangle - \langle l \rangle^2)$ is deduced by taking the mean diameters $l = \langle d_c \rangle$ for various ligaments. Considering a sample of ligaments spread across space and time with different imposed gas flow We , this corrugation factor was determined mostly to be in the range spanning $n = 3 - 8$. The values close to $n = 4$ were identified as the most frequently observed across various We flows. This corresponds to extremely corrugated ligaments and $n = 4$ is a practical limit on the coefficient considering various physical constraints [10]. Also a very low value of $m = 3$ (corresponding to the fit) represent a broad ligament size (l) distribution, as observed from the experiments as well. The invariance with respect to We number supports the saturation of this coefficient to the theoretical limit. Although the sub-secondary breakup process involves the ligament production through various mechanism, the ligaments collectively are postulated to exhibit extreme levels of corrugations, primarily due to the highly potent disruptive aerodynamic forces at extreme We . The ligaments are expected to scale down to smaller average diameters as We is increased (as observed in the experiments in Fig. 5), but the shape factor is already saturated to the limit and depicts values near $n = 4$. To elucidate this hypothesis, we will consider the estimated size distribution in the subsequent sections.

D. Droplet size distribution

The unsteady imposition arising from the open nozzle-blast wave induced flows [28], the dynamics are expected to be transient. However the droplet aerobreakup intrinsically is a transient phenomenon. The recurrent wave cascade continuously strips away the liquid from the parent droplet mass and generates droplets through sub-secondary breakup processes. Hence the droplets are produced with different characteristics over a period of time. To capture this effect, droplet size measurements were performed considering the time stamp (t^*) of their appearance in the measurement zone. This zone was located $30mm$ downstream from the droplet for better visibility [14].

All the sampled droplets, when consolidated, gave the overall size distributions for different We flow. However, the appearance of the first and the last droplet in the zone reflects the breakup time period t_b^* , which can be subdivided into equal sub-periods. The assessment of size distributions in these periods enables the determination of transient characteristics of the system. The time scale t^* , measured from the appearance of the first droplet, is then normalized using the breakup period t_b^* such that $\tau_b = t^*/t_b^*$. The overall distributions as probability density functions (PDFs) are illustrated in Fig. 8a. The average droplet size decreases as We is increased. The transient PDFs are represented as a contour plot depicting a transition to observing larger droplet sizes as time progresses in Fig. 8b. However, if we normalize the PDFs with corresponding average droplet size d_{10}^* , we observe the different time periods follows same distributions. The same effects are visible in all We discussed in this study as illustrated in Fig. 8c.

For more reliable statistics with a larger sample size in each period, the breakup time is split into 3 parts, and the corresponding normalized PDFs along with global distributions are presented in in Fig. 9a along with the compound gamma and log-normal distribution fits. They almost overlap, especially till $d/\langle d \rangle \approx 6$. The compound gamma distribution aligns with the earlier prediction $n = 4$, deduced from the ligament-mediated mechanism. The deviation is observed consistently at the tails, which might be due to the effects like (i) The unsteady decaying airflow with

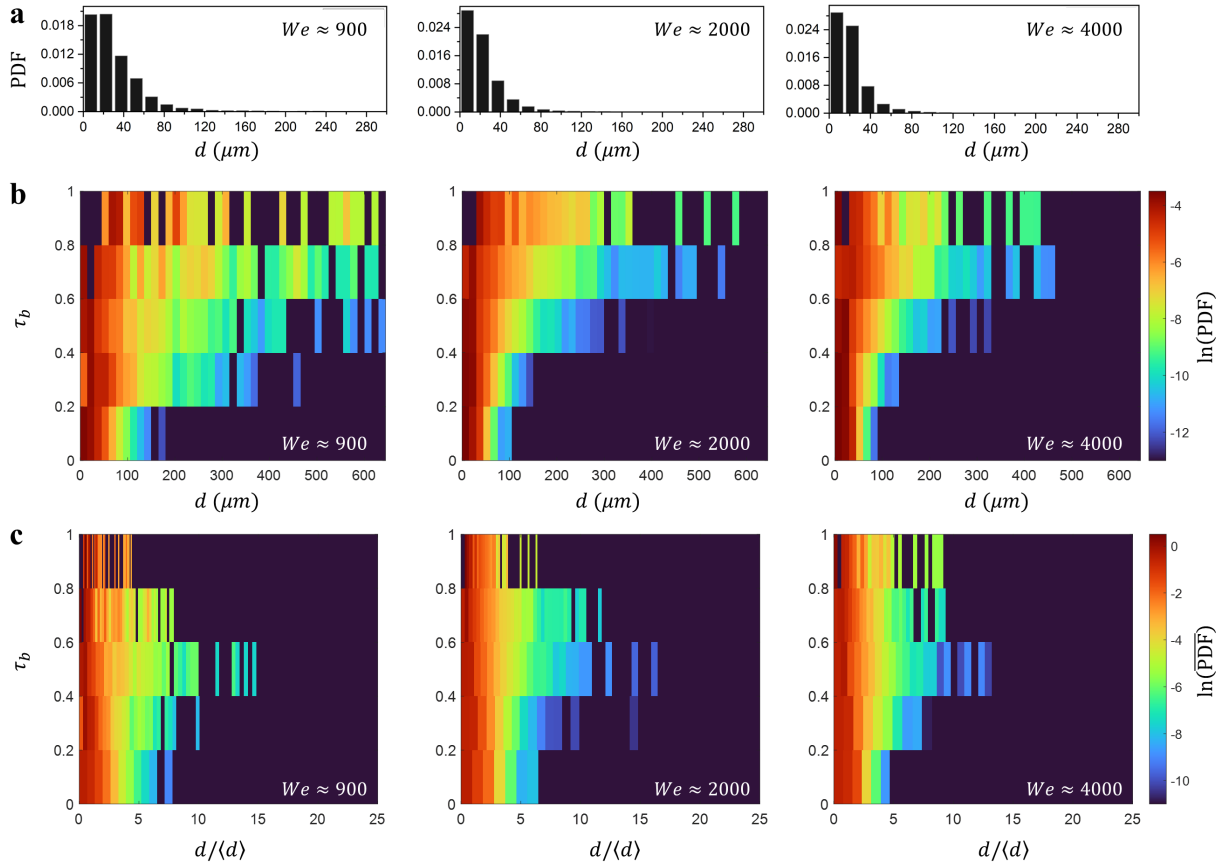


FIG. 8. (a) Overall droplet size distribution PDFs at different We . (b) Temporal evolution of PDFs represented a contour plot, where the breakup event is subdivided into 5 equal periods. (c) Temporal evolution of Normalised PDFs (using average droplet diameter $\langle d \rangle$), depicting self-similar behaviour in time. Here τ_b =centre of each time period/total breakup time.

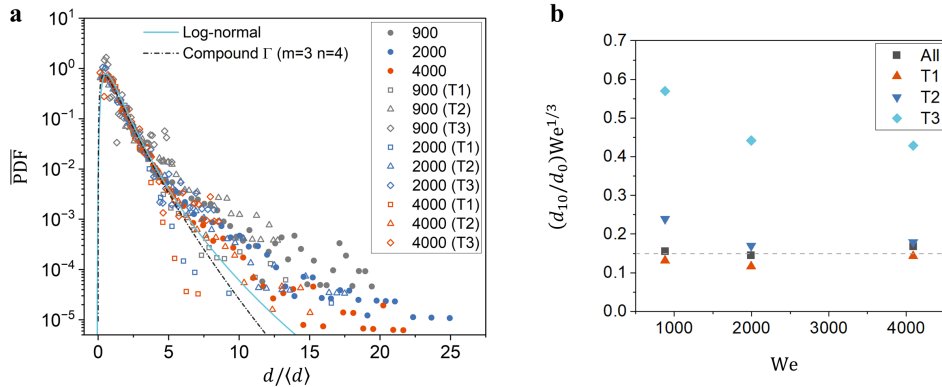


FIG. 9. Normalized PDFs depicting self-similar distributions across We and time (T1-T3) denotes equal breakup periods). (b) Invariance of We based normalized average diameters.

lower effective We at later stages generating larger droplets produced from the residual parent droplet and (ii) coalescence of daughter droplets. To have a better understanding, we require unsteady destabilization models and better measurement capabilities.

Since the normalized PDFs follow a common underlying distribution, the prediction of average diameter is ideally sufficient to determine actual PDFs. A previous study [29] assumed a chaotic isotropic deformation of the liquid mass to analytically deduce size distributions in explosive breakups. We extend the same to present catastrophic aerobreakup. The imposed disruptive energy E induces a deformation rate of $\dot{\gamma}$ to the droplet of initial radius r_0 ,

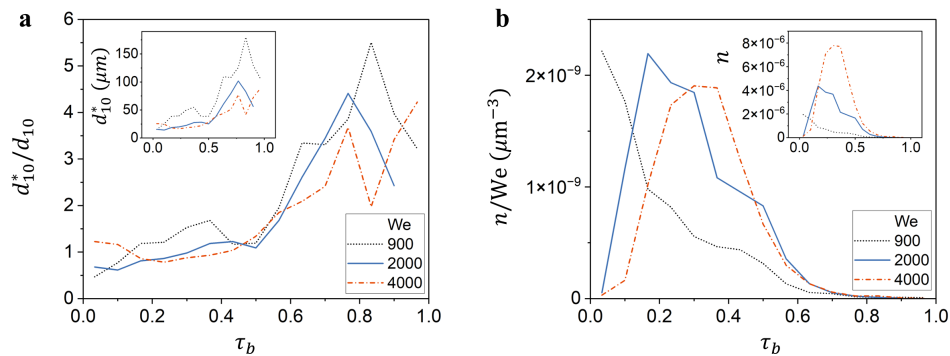


FIG. 10. Transient evolution of (a) average diameter of daughter droplets. (b) volumetric concentration of droplet frequency. They are normalized using scales based on catastrophic breakup assumption. The insets denotes non-normalized counterparts.

such that $(1/2)\rho_l r_0^2 (\dot{\gamma} r_0)^2 \sim E$. Assuming chaotic random dispersal of energy [29], the same deformation rate is extended to individual daughter droplets with characteristic size r_f (radius), such that the associated incremental surface energy scales as $(1/2)\rho_l r_f^2 (\dot{\gamma} r_0)^2 \sim \sigma r_f^2$. Simplifying these equations where $E \sim \rho_a u_a^2 r_0^3$ for aerobreakup, we get $(r_f/r_0) \sim We^{-1/3}$. Suspecting $d_{10} \sim d_f$, we have

$$d_{10}/d_0 \sim We^{-1/3} \quad (3)$$

This scaling relationship is validated in Fig. 9b. Although the observed breakup is not completely random, the hypothesis holds. Deviations from this are expected at lower We , where the breakup is evidently regular in geometry and anisotropic. A similar scaling law for average droplet diameters was deduced for flat-fan sprays, using the unstable wave-mediated sheet disintegration mechanism [9].

A temporal evolution of average droplet diameters d_{10}^* are also presented in Fig. 10a, where global averages d_{10} is used to normalization, depicting a similar trend for different We , where smaller droplets appear first (also see Fig. 8b). The possible mechanisms include: (i) unsteady impulsive airflow with higher effective We generating smaller droplets during early interaction (ii) size dependent migration where smaller droplets with lower inertia reach the measurement zone first. The number of daughter droplets N can be also deduced extending earlier analysis

$$N \sim (r_0^3/r_f^3) \sim We \quad (4)$$

We consider the number of droplets produced per unit measurement volume i.e. the number concentration $n = N/V_{meas}$ for unbiased estimates of droplet count [14, 30]. Temporal evolution of the normalized version n/We is plotted in Fig. 10b illustrating the validity of aforementioned scales. A similar trend is observed for different We , where a huge number of droplets are generated in the early stages. Culminating both the ideas (temporal evolution of d_{10}^* and n), we deduce that the droplets with smaller droplets appear first in large quantities. Since, we observe an insignificant variation in d_{10}^* evolution at all We (see inset of Fig. 10a), it suggests that the overall size distributions is prominently determined by the scale of n maxima (see inset of Fig. 10b).

IV. CONCLUSION

In the present study, we have a closer look into the intermediate sub-scale processes that occur during the unsteady aerobreakup of a droplet in the range $We \approx 900 - 4000$ using a shock tube system. The subsequent multi-scale interfacial deformations, originating from various unstable wave mechanisms (KHI, RTI and RPI), forms a non-linear cascade. The undulations disintegrate through sub-secondary breakup processes, primarily conforming to a ligament or bag mode. The daughter droplet size distributions were estimated using a DFD technique, where the normalized distributions, at different We and time periods, followed a common fit. This compound gamma distribution parameter aligns well with the coefficient determined from terminal ligaments. This corresponds to the limit associated with most extreme corrugations physically possible. This illustrates a self-similar behavior pertaining the size distributions as well as the evolution of topological features at different scales (initial droplet/undulation; global/local) with an effective We bridging them.

ACKNOWLEDGMENTS

S.J.R. acknowledges the support through the Prime Minister's Research Fellowship (PMRF).

-
- [1] S. Sharma, N. K. Chandra, S. Basu, and A. Kumar, Advances in droplet aerobreakup, *The European Physical Journal Special Topics* 10.1140/epjs/s11734-022-00653-z (2022).
 - [2] D. R. Gueldenbecher, C. López-Rivera, and P. E. Sojka, Secondary atomization, *Experiments in Fluids* **46**, 371 (2009).
 - [3] T. Theofanous, Aerobreakup of Newtonian and Viscoelastic Liquids, *Annual Review of Fluid Mechanics* **43**, 661 (2011).
 - [4] A. Zandian, W. A. Sirignano, and F. Hussain, Length-scale cascade and spread rate of atomizing planar liquid jets, *International Journal of Multiphase Flow* **113**, 117 (2019).
 - [5] A. Zandian, W. A. Sirignano, and F. Hussain, Planar liquid jet: Early deformation and atomization cascades, *Physics of Fluids* **29**, 062109 (2017).
 - [6] A. Zandian, W. A. Sirignano, and F. Hussain, Understanding liquid-jet atomization cascades via vortex dynamics, *Journal of Fluid Mechanics* **843**, 293 (2018).
 - [7] Y. Wang, K.-S. Im, and K. Fezzaa, Similarity between the Primary and Secondary Air-Assisted Liquid Jet Breakup Mechanisms, *Physical Review Letters* **100**, 154502 (2008).
 - [8] E. Villermaux, P. Marmottant, and J. Duplat, Ligament-Mediated Spray Formation, *Physical Review Letters* **92**, 074501 (2004).
 - [9] S. Kooij, R. Sijs, M. M. Denn, E. Villermaux, and D. Bonn, What Determines the Drop Size in Sprays?, *Physical Review X* **8**, 031019 (2018).
 - [10] B. Keshavarz, E. C. Houze, J. R. Moore, M. R. Koerner, and G. H. McKinley, Ligament Mediated Fragmentation of Viscoelastic Liquids, *Physical Review Letters* **117**, 154502 (2016).
 - [11] S. Sharma, A. Pratap Singh, S. Srinivas Rao, A. Kumar, and S. Basu, Shock induced aerobreakup of a droplet, *Journal of Fluid Mechanics* **929**, A27 (2021).
 - [12] N. K. Chandra, S. Sharma, S. Basu, and A. Kumar, Shock-induced aerobreakup of a polymeric droplet, *Journal of Fluid Mechanics* **965**, A1 (2023).
 - [13] S. Sharma, N. K. Chandra, A. Kumar, and S. Basu, Shock-induced atomisation of a liquid metal droplet, *Journal of Fluid Mechanics* **972**, A7 (2023).
 - [14] S. Sharma, S. J. Rao, N. K. Chandra, A. Kumar, S. Basu, and C. Tropea, Depth from defocus technique applied to unsteady shock-drop secondary atomization, *Experiments in Fluids* **64**, 65 (2023).
 - [15] J. Hoepffner, R. Blumenthal, and S. Zaleski, Self-Similar Wave Produced by Local Perturbation of the Kelvin-Helmholtz Shear-Layer Instability, *Physical Review Letters* **106**, 104502 (2011).
 - [16] P. Marmottant and E. Villermaux, On spray formation, *Journal of Fluid Mechanics* **498**, 73 (2004).
 - [17] M. Jalaal and K. Mehravaran, Transient growth of droplet instabilities in a stream, *Physics of Fluids* **26**, 012101 (2014).
 - [18] B. Dorschner, L. Biasiori-Poulanges, K. Schmidmayer, H. El-Rabii, and T. Colonius, On the formation and recurrent shedding of ligaments in droplet aerobreakup, *Journal of Fluid Mechanics* **904**, A20 (2020).
 - [19] J. J. S. Jerome, S. Marty, J.-P. Matas, S. Zaleski, and J. Hoepffner, Vortices catapult droplets in atomization, *Physics of Fluids* **25**, 112109 (2013).
 - [20] Y. Wang, R. Dandekar, N. Bustos, S. Poulain, and L. Bourouiba, Universal Rim Thickness in Unsteady Sheet Fragmentation, *Physical Review Letters* **120**, 204503 (2018).
 - [21] I. Oshima and A. Sou, Air-blast atomization of a liquid film, *Journal of Fluid Mechanics* **985**, A36 (2024).
 - [22] I. M. Jackiw and N. Ashgriz, On aerodynamic droplet breakup, *Journal of Fluid Mechanics* **913**, A33 (2021).
 - [23] I. M. Jackiw and N. Ashgriz, Prediction of the droplet size distribution in aerodynamic droplet breakup, *Journal of Fluid Mechanics* **940**, A17 (2022).
 - [24] F. Veron, C. Hopkins, E. L. Harrison, and J. A. Mueller, Sea spray spume droplet production in high wind speeds, *Geophysical Research Letters* **39**, 10.1029/2012GL052603 (2012).
 - [25] Y. Troitskaya, A. Kandaurov, O. Ermakova, D. Kozlov, D. Sergeev, and S. Zilitinkevich, Bag-breakup fragmentation as the dominant mechanism of sea-spray production in high winds, *Scientific Reports* **7**, 1614 (2017).
 - [26] N. K. Chandra, S. Sharma, S. Basu, and A. Kumar, Aerodynamic bag breakup of a polymeric droplet, *Physical Review Fluids* **9**, 113303 (2024).
 - [27] S. Pal, C. Pairetti, M. Crialesi-Esposito, D. Fuster, and S. Zaleski, Statistics of drops generated from ensembles of randomly corrugated ligaments, *Physics of Fluids* **36**, 112116 (2024).
 - [28] G. Vadlamudi, A. Aravind, S. J. Rao, and S. Basu, Insights into spatio-temporal dynamics during shock-droplet flame interaction, *Journal of Fluid Mechanics* **999**, A22 (2024).
 - [29] F. M. Sultanov and A. L. Yarin, Droplet size distribution in a percolation model for explosive liquid dispersal, *Journal of Applied Mechanics and Technical Physics* **31**, 10.1007/BF00852443 (1990).
 - [30] S. J. Rao, S. Sharma, S. Basu, and C. Tropea, Depth from defocus technique: a simple calibration-free approach for dispersion size measurement, *Experiments in Fluids* **65**, 55 (2024).